



## ARCHIVIO ISTITUZIONALE DELLA RICERCA

### Alma Mater Studiorum Università di Bologna Archivio istituzionale della ricerca

Image enhancement variational methods for Enabling Strong Cost Reduction in OLED-based Point-of-Care Immunofluorescent Diagnostic Systems

This is the final peer-reviewed author's accepted manuscript (postprint) of the following publication:

*Published Version:*

Image enhancement variational methods for Enabling Strong Cost Reduction in OLED-based Point-of-Care Immunofluorescent Diagnostic Systems / Damiana, Lazzaro; Serena, Morigi; Melpignano, P.; Loli Piccolomini, E.; Luca, Benini. - In: INTERNATIONAL JOURNAL FOR NUMERICAL METHODS IN BIOMEDICAL ENGINEERING. - ISSN 2040-7939. - STAMPA. - 34:3(2018), pp. 2932-2951. [10.1002/cnm.2932]

This version is available at: <https://hdl.handle.net/11585/614467> since: 2018-03-06

*Published:*

DOI: <http://doi.org/10.1002/cnm.2932>

*Terms of use:*

Some rights reserved. The terms and conditions for the reuse of this version of the manuscript are specified in the publishing policy. For all terms of use and more information see the publisher's website.

(Article begins on next page)

This item was downloaded from IRIS Università di Bologna (<https://cris.unibo.it/>).  
When citing, please refer to the published version.

This is the final peer-reviewed accepted manuscript of:

Lazzaro, D, Morigi, S, Melpignano, P, Loli Piccolomini, E, Benini, L. Image enhancement variational methods for enabling strong cost reduction in OLED-based point-of-care immunofluorescent diagnostic systems. *Int J Numer Meth Biomed Engng*. 2018; 34:e2932.

The final published version is available online at

<https://doi.org/10.1002/cnm.2932>

.

Rights / License: The terms and conditions for the reuse of this version of the manuscript are specified in the publishing policy. For all terms of use and more information see the publisher's website.

# Image Enhancement Variational Methods for Enabling Strong Cost Reduction in OLED-based Point-of-Care Immunofluorescent Diagnostic Systems

D. Lazzaro, S. Morigi\*, P. Melpignano,  
E. Loli Piccolomini, L. Benini

*Department of Mathematics, University of Bologna, Bologna, Italy,*

*Department of Electrical, Electronic, and Information Engineering, University of Bologna, Bologna, Italy,*  
*Or-el d.o.o. Organska elektronika, Kobariid, Slovenia.*

## SUMMARY

**Objective:** Immunofluorescence diagnostic systems cost is often dominated by high-sensitivity, low-noise CCD-based cameras which are used to acquire the fluorescence images. In this paper we investigate the use of low-cost CMOS sensors in a point-of-care immunofluorescence diagnostic application for the detection and discrimination of four different serotypes of the Dengue virus in a set of human samples. **Methods:** A two-phase post-processing software pipeline is proposed which consists in a first image enhancement stage for resolution increasing and segmentation, and a second diagnosis stage for the computation of the output concentrations. **Results:** We present a novel variational coupled model for the joint super-resolution and segmentation stage, and an automatic innovative image analysis for the diagnosis purpose. A specially designed Forward Backward-based numerical algorithm is introduced and its convergence is proved under mild conditions. We present results on a cheap prototype CMOS camera compared with the results of a more expensive CCD device, for the detection of the Dengue virus with a low-cost OLED light source. The combination of the CMOS sensor and the developed post-processing software allows to correctly identify the different Dengue serotype using an automatized procedure. **Conclusions:** The results demonstrate that our diagnostic imaging system enables camera cost reduction up to 99%, at an acceptable diagnostic accuracy, with respect to the reference CCD-based camera system. The correct detection and identification of the Dengue serotypes has been confirmed by standard diagnostic methods (RT-PCR and ELISA). Copyright © 0000 John Wiley & Sons, Ltd.

Received ...

**KEY WORDS:** Variational image processing, image segmentation, image super-resolution, immunofluorescence technique, CMOS image sensors

## 1. INTRODUCTION

Among several areas of applications of image sensors, a significant field is fluorescence microscopy. Imagers can be used in different contexts: from the visualization of particular features in cell cultures to the detection of fluorescent spots in experiments of indirect immunofluorescence, where the detection of the fluorescent optical signal allows to determine the presence of antibodies against a certain pathogen in the biological fluid under analysis [17, 20]. The immunofluorescence technique is currently applied in human medical diagnostic but can be applied also to other diagnostic fields, ranging from veterinary medicine to environmental science, from water analysis to nutritional studies. Recently, this technique has been applied in the development of a multi-parametric

---

\*Correspondence to: serena.morigi@unibo.it

diagnostic point-of-care system based on OLED [28, 27]. While biological and chemical sensors based on OLED have already been presented in literature ([33, 6, 1, 32] and ref. therein), the most of them are mono parametric and the detection of the fluorescent signal is performed with a photo diode (organic or silicon based) which could also be directly integrated to the disposable bio-chip. Moreover, in standard protein or DNA micro-array the fluorescence excitation is obtained scanning a laser beam through the bio-probes matrix and collecting the signal with a photo-multiplier or using a high sensitivity scientific CCD camera. In the diagnostic system that we will consider in this paper a different approach has been considered. In particular, a matrix of different antigens has been deposited (in drops of  $1\ \mu\text{l}$  each) on a transparent plastic substrate. After the reaction with the biological fluid under analysis and a second reaction with a fluid containing secondary antibodies tagged with a fluorophore, the fluorescent signal of the bounded region in the probe matrix has been excited by the OLED, using the same parameters as described in [28, 27]. The weak fluorescence signal emitted by the excited fluorophore was then collected by a high sensitivity scientific CCD camera. The image was then manually segmented in order to separate the salient foreground from the noisy background, and finally the task of detection of the intensity of the region of interest as a measure of the presence of the antibodies against the specific disease in the biological sample was realized by human experts.

The depicted state-of-the-art Immunofluorescent Diagnostic System presents two main disadvantages: a high cost due to the CCD camera used and a time consuming procedure due to the involvement of human experts.

The main contributions of this paper are summarized as follows.

- We design a low-cost diagnostic imaging system by replacing the expensive CCD cameras with a cheaper CMOS imaging sensor, equipped with a post-processing software framework which can guarantee the same accuracy results;
- We propose a novel variational model which integrates super-resolution and segmentation for the first stage of the post-processing software framework with an automatic parameter selection.
- We introduce an automatic diagnosis procedure for a quick, standard and reliable computer-aided diagnosis imaging system.

Such an automatic diagnosis procedure can also allow an increased flexibility in the antigen spots positioning in the matrix for creating a low-cost point-of-care device by avoiding, for example, the use of an expensive mechanical robot that arranges with high spatial precision several antigen spots in the matrix. For this purpose, recently, some companies, such as *Or-el d.o.o.* proposed to replace the highly expensive CCD camera with cheaper CMOS cameras. It is the first time, to our best knowledge, that a low cost and compact CMOS detector is used for fluorescence signal detection and quantification in an OLED-based low density protein micro-array bio-chip. This solution allows for an improved miniaturization of the integrated fluorescence reader system opening the way to fast, cheap and accurate measure of low density multi-parametric protein or DNA micro array, ideal to be used in hand-held portable point-of-care diagnostic systems. However, the use of a CMOS camera is subjected to well-known issues. In general, CMOS cameras provide noisier images, and some cameras, in order to limit the cost, strongly reduce the resolution of the image. For this reason a post-processing phase on an image acquired by a CMOS camera is required to overcome these problems and produce diagnostic results comparable to those produced by a CCD camera, thus encouraging the usage of these low-cost image devices in a fluorescence microscopy context. The proposed diagnostic imaging system, starting from the detected fluorescence signal captured by the CMOS sensor, named fluo-image in the following, permits to produce automatic output results for the identification of the kind of pathogen present in the biological sample and for the quantification of the antibody concentration in the sample under analysis. We follow a pipeline strategy: in the first stage the corrupted fluo-image undergoes to a super-resolution and segmentation procedure which allows for the extraction of salient spots of interests, which will be analyzed in the second stage in terms of intensity distribution and shape for the identification of the kind of pathogen present and the quantification of its concentration in the sample.

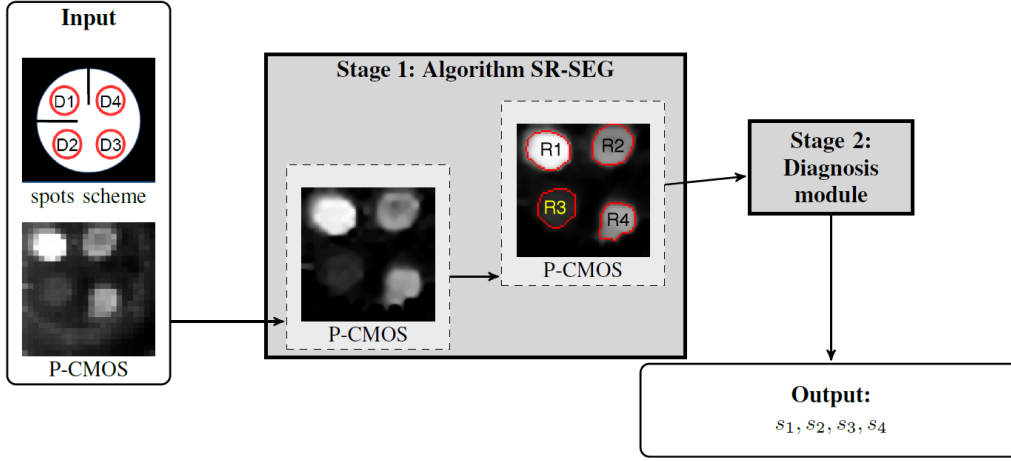


Figure 1. Pipeline of the diagnostic imaging system: image super-resolution and segmentation (Stage 1), and diagnosis (Stage 2).

In the following we first introduce in Section 2 the methodological overview, then in Section 3 we briefly describe some related work about both the OLED-based diagnostic system, and the image processing methods. In Section 4 we present the proposed coupled variational model for super-resolution and image segmentation which realizes Stage 1 of our diagnostic imaging system. In particular, we first describe the mathematical model providing theoretical results on its resolvability in Section 4.1, the numerical solution is derived in Section 4.2 by an iterative forward-backward type strategy which is proved to converge under mild conditions, and finally we summarize the algorithm in Section 4.3. In Section 5 we present the validation of the proposed diagnostic imaging system. More precisely, we evaluate the performance of Algorithm SR-SEG for super-resolution and segmentation in Sections 5.2 and 5.3, respectively, and in Section 5.4 we show the performance of the overall processing chain based on the analysis of the suitable metrics proposed in Section 5.1. Finally, in Section 6 we draw our conclusions and some possible future developments.

## 2. METHODS

In our experiments, we will consider a new kind of serological diagnostic for the detection and discrimination of the four different serotypes of the Dengue virus in a set of human samples [14]. In these experiments a matrix of four spots, each corresponding to a specific Dengue serotype, has been deposited on a transparent substrate for the reaction with human sera. It should be noted that the four Dengue serotypes can present a problem of cross-reactivity so it is possible to have more than one fluorescent spot in the same matrix, but the brightest spot intensity allows to determine the specific serotype present in the patient blood. In particular, we investigate the performance of a prototype CMOS cameras, where samples are subjected to an OLED illumination, based on a large-pixel, low-cost CMOS sensor, comparing them to the same sample images acquired by a unique CCD reference camera (Hamamatsu C8484-03G). Some features extracted from the data sheets of the two considered cameras are reported in Table I.

Compared to the high-cost CCD camera (the price of the CCD camera used in our tests is about €10 000), the prototype considered CMOS device is cheaper and around €100. We remark that commercial CMOS camera prices range in the order of few thousands Euros. In this work we demonstrate that a post-processing procedure enables automatic computer-aided diagnosis with a significant decrease of costs based on robust, efficient and reliable variational methods.

In Fig. 1 we illustrate the pipeline of the overall automatic Immunofluorescent Diagnostic Imaging System. The images acquired by the low-cost devices, such as the P-CMOS camera do not present

Table I. Some features of the CCD and P-CMOS devices.

	Hamamatsu ORCA-03G	Prototype camera
Imaging device	CCD	CMOS
Pixels number	$1344 \times 1024$	$24 \times 24$
Image size	$168 \times 128$ (binning 8)	$24 \times 24$
Cell size (in $\mu m$ )	$6.45 \times 6.45$	$130 \times 130$
Effective area (in $mm$ )	$8.67 \times 6.60$	$3.12 \times 3.12$
Frame rate (full res.)	8.9 frames/s	-
A/D converter	12 bit	12 bit
Full well capacity	15 000 e	-
Dynamic range	2142:1	> 85dB
Exposure time	10 s to 10 s (rapid rolling mode)	100 $\mu s$ to 100 s
Operating ambient temp.	0°C to +40°C	-15°C to +85°C
Power requirements	DC 12 V, 50/60 Hz	5.0 V
Power consumption	24 VA	< 30mW
Cost	$\sim \text{€}10\,000$	$\sim \text{€}100$

an accentuated degradation caused by noise. However, the super-resolution process is strongly suggested for the success of the application of the segmentation tools.

In Stage 1, the low resolution captured fluo-image undergoes a background subtraction and a joint super-resolution and segmentation process which enlarges the image and produces four segmented regions  $R_1, R_2, R_3, R_4$ . This holds the potential to avoid failures in segmentation due to excessively coarse or rough boundaries and makes the entire process automatic, robust and efficient.

The four segmented regions are processed in Stage 2 by the diagnosis module illustrated in Fig.1, which detects both the order of intensities and the quantitative measures of the associated concentrations  $s_1, s_2, s_3, s_4$ . More precisely, the four segmented regions are processed by computing the intensity mean value of the pixels for each region thus identifying both the order of brightness and the concentration associated with each spot. Consequently, the brightest spot intensity allows to determine the specific serotype present in the patient blood. In particular, we applied the imaging system to the serological diagnostic for the detection and discrimination of the four different serotypes of the Dengue virus, denoted by D1, D2, D3, and D4 in Fig.1, in a set of human samples.

### 3. RELATED WORKS

#### 3.1. Related work on OLED based bio-sensors

The first researches on OLED based bio-sensors have been made by two different research groups: the Donald Bradley group from Imperial College London, [21], and the Ruth and Joseph Shinar group from Ames Laboratory-USDOE Iowa State University, [35]. They investigated first the use of OLEDs as integrated light source in different kinds of biological sensor based on fluorescence detection of tagged probes. After these pioneering works, other groups worldwide have followed this approach, see [33, 32, 1], concentrating their attention on liquid or gas flow based systems, where the samples and the fluorescent probes are dispersed, allowing the detection of a single biological parameter. In these studies, a strong attention to the bio-sensor integration was paid and the OLED was integrated into the biosensor together with the light detection system, normally a photodiode (organic or silicon based) and cannot be re-used for other analysis. Moreover, the sensitivity of these bio-sensors was rather low. More recently, authors in [28, 27] have demonstrated the feasibility of an OLED-based biochip using a protein (or a DNA) micro-array integrated with a properly optimized OLED source. This configuration is suitable for a multiparametric diagnostic test. In latter studies, an OLED source, specifically optimized in term of spectral emission tuned with the fluorophore absorption, has allowed to obtain a high bio-detection sensitivity. For all these experiments a high

sensitivity CCD camera was used as high resolution detector. A similar idea was also followed in [24], which have also adopted a multiplex detection of a biological probes array always using an OLED as fluorescence excitation source. In their experiments they have used a photodiode array to detect the light emitted by the different fluorescent spots. However this system present a limited spatial resolution and is limited by the number of photodiodes that can be used in the detection system. As an evolution of the studies described in [28, 27], the research presented in this paper aims at substituting the expensive and bulk high sensitivity CCD camera with a cheaper and smaller CMOS sensor, preserving the diagnostic sensitivity and allowing a cost reduction of the diagnostic point-of-care reader. In our system the OLED is not anymore integrated in the biosensor, being its lifetime sufficiently long to perform several analysis. Rather, it is fitted to the portable reader used to read the transparent substrate, where the protein or DNA micro-array are arranged.

### 3.2. Related work on Image Super Resolution

Single Image Super Resolution (SISR) is an inverse problem which aims to estimate a High Resolution (HR) image from a single Low Resolution (LR) image. Existing methods to solve SISR problem can be classified in four categories. *Interpolation based algorithms*, ranging from the classical nearest neighbour, bilinear and bicubic interpolation, estimate the unknown pixels in HR grids by using an analytical representation in a specific base. Their drawbacks, as oversmoothing, ringing and jaggies artifacts, have been partially overcome using a priori edge knowledge on the image [25, 7]. *Example-Based SISR methods* learn the high frequency details lost in the input LR image from a training database-image composed by LR and HR image pairs and their performance heavily depends on the correlation between test images and training database [23]. *Sparse representation-based algorithm* are inspired by similarity of sparse representations of LR and HR images, considering an appropriately chosen over-complete dictionary. This is usually based on seeking for a sparse representation for each patch of the low-resolution input, whose coefficients are then used to generate the high-resolution output, [37, 13]. *Reconstruction-based algorithms* enforce the consistency between the blurred and dowsampled version of the estimated HR image and the observed LR image (fidelity term), imposing the well- posedness of the solution by a proper regularizer (regularization term) in a variational framework.

The super-resolution strategy that we proposed and integrated in the diagnostic imaging system can be classified as a reconstruction-based method.

### 3.3. Related work on Image segmentation

Image segmentation is a relevant problem in the understanding of biological vision. There exist many different way to define the tasks of segmentation (template matching, component labelling, thresholding, boundary detection, quad-trees, texture segmentation) and there is no universally accepted best segmentation procedure.

The methods range from the simplest and classical region-based segmentation methods and Otsu's methods [18], to the more efficacy and sophisticated variational methods, recently proposed in literature. Among the variational segmentation models, the most popular are the Mumford-Shah non-convex piecewise constant and smooth models [31]. A variety of methods have been developed to generalize it. The segmentation method recently proposed by Cai, Chan and Zeng in [5] aims to minimize a convex version of the Mumford-Shah functional by finding an optimal approximation of the image based on a piecewise smooth function. Another very popular relaxation method of the Mumford-Shah functional is the so-called method of active contours without edges (Chan-Vese model) introduced in [9] which seeks for an approximation of a given image with a piecewise constant representation.

The segmentation method we proposed relies on the variational model introduced in [5], combining it with a super-resolution strategy.



#### 4. THE JOINT SUPER-RESOLUTION AND SEGMENTATION MODEL

##### 4.1. The variational model

For our diagnostic imaging system we propose a coupled super-resolution and segmentation approach which relies on a variational model to solve an inverse super-resolution problem and on image thresholding to derive segmentations from the recovered piecewise smooth image. The key idea of the method is that one can obtain a good segmentation by properly thresholding a piecewise smooth and enlarged approximation of the given LR image  $g$ .

To the best of our knowledge this is the first variational model with this main goal to achieve. From a mathematical point of view the functional to be minimized is a three terms convex functional which, at the first glance, differs from the proposal in [5] only for the two regularization parameters, which in our case, are chosen to be a space-variant function and an automatically selected parameter. However, since the operators involved, the mathematical meaning of the terms is quite different, thus strongly affecting the resolvability of the model, and also the numerical implementation is different.

The input in our proposal is a LR given image and the solution of the optimization problem produces a HR piecewise smooth image. In particular, using the lexicographically stacked representation of an image, the relationship between the original HR image  $u \in \Omega_H = \mathbb{R}^{N^2 \times 1}$  and the LR observation  $g \in \Omega_L = \mathbb{R}^{n^2 \times 1}$  obtained by an up-sampling factor  $s > 1$ , that is  $N^2 = s^2 n^2$ , can be mathematically modeled as:

$$g = D B u + \zeta = A u + \zeta \quad (1)$$

where  $B \in \mathbb{R}^{N^2 \times N^2}$  is the space invariant point spread function of the camera for the LR image,  $D \in \mathbb{R}^{n^2 \times N^2}$  is the subsampling matrix,  $A \in \mathbb{R}^{n^2 \times N^2}$  represents the global linear operator linking the HR image and the LR image, and  $\zeta$  denotes the noise, which is assumed as an unknown additive white Gaussian noise.

The key step in our model is solving a minimization problem of the form

$$u^* \in \arg \min_{u \in \Omega_H} \left\{ \mathcal{F}(u; \lambda) = \frac{1}{2} \|A u - g\|_2^2 + \lambda \|L u\|_1 + \|E^{1/2} L u\|_2^2 \right\} \quad (2)$$

where  $\lambda > 0$  is a scalar parameter,  $L := [L_1 \ L_2]^T$ ,  $L_1, L_2 \in \mathbb{R}^{N^2 \times N^2}$  is the  $2N^2 \times N^2$  linear operator with  $L_1, L_2$  first-order difference operators along the horizontal and vertical directions,  $E \in \mathbb{R}^{2N^2 \times 2N^2}$  is a diagonal matrix  $E := \text{diag}(\eta_1, \dots, \eta_{N^2}, \eta_1, \dots, \eta_{N^2})$ , with positive scalar elements  $\eta_i$  specified below. The first regularization term  $\|L u\|_1$  represents the classical Total Variation (TV) seminorm [26], that is the  $\ell_1$ -norm of the image gradient magnitude defined as follows

$$\|L u\|_1 := \sum_{i=1}^{N^2} \|(L u)_i\|_2 = \sum_{i=1}^{N^2} \sqrt{(L_1 u)_i^2 + (L_2 u)_i^2}, \quad (3)$$

while the second regularization term reads as follows

$$\|E^{1/2} L u\|_2^2 = \sum_{i=1}^{2N^2} \eta_i (L u)_i^2. \quad (4)$$

The fidelity term in (2) imposes the consistency between the reconstructed HR image and the observed LR image, the first regularization term penalizes the length of the region boundaries, and the second one smooths the inner regions. The role of  $E$  is to preserve the boundaries of the segmented regions while allowing to smooth the interior parts, as in the original Mumford-Shah segmentation model [31]. For this purpose, we define the function  $\eta : \mathbb{R}^+ \rightarrow [0, 1]$  as follows

$$\eta(s) := \frac{1}{1 + \left(\frac{s}{\tau}\right)^2}, \quad (5)$$



with a given parameter  $\tau > 0$ , which acts as an edge detector operator when applied to  $s_i = \|(Lu)_i\|_2^2$ . Therefore the diagonal elements of  $E$  are  $\eta_i = \eta(s_i)$ ,  $i = 1, \dots, N^2$  and represent space-variant regularization parameters.

The  $\ell_1$ -norm is classically used as regularization term since among convex regularizers it induces sparsity most effectively. This choice is motivated by the fact that in our application context the fluo-images are characterized by strong gradient sparsity.

Once the HR image  $u^*$  is computed by solving (2), then the final segmentation is simply given by thresholding  $u^*$  into different regions. The thresholds can be given by the users or can be obtained automatically using any clustering methods. In our immunofluorescent context the threshold values are automatically given according to sensitivity of the acquisition device, thus the super-resolution segmentation model (2) can be classified as un-supervised, where the number of regions is not fixed in advance. As a consequence, problem (2) does not need to be solved again when the number of regions required is changed.

In the following proposition we first prove that problem (2) admits at least one solution, then, in Section 4.2 we provide an efficient algorithm to determine an approximate solution.

*Proposition 1*

For a given parameter  $\lambda > 0$ , the minimization problem (2) admits at least one solution.

*Proof*

The first term  $\frac{1}{2}\|Au - g\|_2^2$  in (2) is continuous and coercive and, moreover, being  $A$  obtained by downsampling the blurring matrix  $B$ , it holds that  $\mathbf{1} \notin \text{Ker}(A)$ , where  $\mathbf{1}$  denotes the vector with all entries equal to 1, and  $\text{Ker}(A)$  is the null space of  $A$ . It follows that

$$\text{Ker}(A) \cap \text{Ker}(L) = \{0\}, \quad (6)$$

where  $\text{Ker}(L)$  is the null space of the gradient operator  $L$ , namely the space of the constant vectors. Note that the scalar factor  $E^{1/2}$  does not affect  $\text{Ker}(L)$ . Then, by Proposition 2.1 in [10] we can conclude that  $\mathcal{F}(u; \lambda)$  is coercive and the set of minimizers of  $\mathcal{F}(u; \lambda)$  is nonempty.  $\square$

#### 4.2. Applying a Forward Backward scheme for the numerical solution

The proposed model (2) is convex, but nonsmooth, thus for its numerical solution we resort to an iterative Forward-Backward (FB) scheme. For this purpose, we rewrite model (2) as follows:

$$u^* \in \arg \min_{u \in \Omega_H} \{\mathcal{F}(u; \lambda) = \mathcal{H}(u) + \mathcal{R}(u)\}, \quad (7)$$

where  $\mathcal{H}(u) = \frac{1}{2}\|Au - g\|_2^2 + \|E^{1/2}Lu\|_2^2$  and  $\mathcal{R}(u) = \lambda\|Lu\|_1$ , and we assumed  $E$  is a diagonal matrix of positive constant values.

$\mathcal{H}(u)$  is smooth, convex and continuously differentiable with  $\ell$ -Lipschitz continuous gradient:

$$\|\nabla \mathcal{H}(u) - \nabla \mathcal{H}(z)\|_2 \leq \ell \|u - z\|_2, \quad u, z \in \Omega_H,$$

and  $\mathcal{R}(u)$  is nonsmooth and convex.

For any vector  $z \in \Omega_H$  and  $\beta > 0$ , we consider the following quadratic approximation of  $\mathcal{H}(u)$  at  $z$  in the objective functional  $\mathcal{F}(u, \lambda)$  in (7):

$$\mathcal{Q}(u, z) = \mathcal{H}(z) + \langle u - z, \nabla \mathcal{H}(z) \rangle + \frac{1}{2\beta} \|u - z\|_2^2 + \mathcal{R}(u) \quad (8)$$

which is equivalent to

$$\mathcal{Q}(u, z) = \mathcal{H}(z) + \frac{1}{2\beta} \|u - (z - \beta \nabla \mathcal{H}(z))\|_2^2 - \frac{\beta}{2} \|\nabla \mathcal{H}(z)\|_2^2 + \mathcal{R}(u). \quad (9)$$

A minimizer of (9) at  $u$  is iteratively determined by setting  $z = u^{k-1}$  in  $\mathcal{Q}(u, z)$ , and ignoring  $u$ -independent terms, thus obtaining the *Backward Step*

$$\begin{aligned} u^k &= \arg \min_{u \in \Omega_H} \mathcal{Q}(u, u^{k-1}) \\ &= \arg \min_{u \in \Omega_H} \left\{ \mathcal{R}(u) + \frac{1}{2\beta} \|u - v^k\|_2^2 \right\} \\ &= \text{prox}_{\beta \mathcal{R}}(v^k), \end{aligned} \quad (10)$$

where  $v^k$  is updated by the explicit *Forward Step*

$$v^k = u^{k-1} - \beta \nabla \mathcal{H}(u^{k-1}) \quad (11)$$

with

$$\nabla \mathcal{H}(u^{k-1}) = A^T (A u^{k-1} - g) + L^T E^{k-1} L u^{k-1}. \quad (12)$$

and  $E^{k-1}$  is the  $E$  matrix where the elements are evaluated on the solution  $u^{k-1}$  obtained at the previous iteration.

Observing that the Backward Step (10) consists in a standard  $\ell_2$ -TV denoising, we can efficiently compute it by using the dual approach in [8] or by the more efficient Alternating Directions Method of Multipliers algorithm [4].

We now analyze convergence of the proposed FB-based minimization approach, whose main computational steps are reported in Section 4.3.

The convergence of a generic Forward-Backward iterative scheme is proved for the problem

$$\min_u \{ \mathcal{H}(u) + \mathcal{R}(u) \} \quad (13)$$

under the following assumptions

- A1)**  $\mathcal{H}(u)$  and  $\mathcal{R}(u)$  are two proper, lower semicontinuous convex functions;
- A2)**  $\mathcal{H}(u)$  is differentiable with  $\ell$ -Lipschitz continuous gradient;
- A3)**  $\mathcal{H}(u) + \mathcal{R}(u)$  is coercive;
- A4)**  $\beta \in (0, \frac{2}{\ell})$  (see also [15], Chapter 12 and references therein).

More precisely, the above convergence result is proved in [11] when the proximity operator is available in exact form, and in [36, 3] when it can only be computed up to a certain precision, as in our case.

In the following proposition we provide the conditions under which the above assumptions A1)-A4) hold, thus proving the convergence of the proposed FB-scheme (11)-(10) for the solution of the optimization problem (2).

#### Proposition 2

For a fixed  $E$ , the iterative FB-scheme (11)-(10) converges to at least one solution of (2) for  $\beta \in (0, \frac{2}{\ell})$  where  $\ell = \lambda_{\max}(A^T A + L^T E L)$ , and  $\lambda_{\max}(\cdot)$  denotes the maximum eigenvalue.

#### Proof

By Proposition 1 it follows that  $\mathcal{H}(u) + \mathcal{R}(u)$  is coercive. Moreover, using (12), we easily obtain that

$$\|\nabla \mathcal{H}(u) - \nabla \mathcal{H}(z)\|_2 = \|(A^T A + L^T E L)(u - z)\|_2 \leq \|(A^T A + L^T E L)\|_2 \|u - z\|_2. \quad (14)$$

Since the elements of the matrix  $E$  are positive, matrix  $(A^T A + L^T E L)$  is positive, semi-definite and symmetric, then  $\|\cdot\|_2 = \lambda_{\max}(\cdot)$ , hence the Lipschitz constant of the operator  $\mathcal{H}(u)$  is  $\ell = \lambda_{\max}(A^T A + L^T E L)$ .  $\square$

#### 4.3. Algorithm SR-SEG

In the following we describe in detail Algorithm SR-SEG which represents the numerical solution of stage 1 in the diagnostic imaging system. In particular, in Algorithm SR-SEG first part (outer loop), we report the main steps of the proposed FB-based iterative scheme used to determine an approximate solution  $u^{k+1}$  of the minimization problem (2). Finally, in the last step, the boundaries of the segmented regions are evaluated by thresholding  $u^{k+1}$  into  $K$  regions.

The Algorithm uses the LR image  $g$  to provide the enlarged image  $u^0 = A^T g$  as the initial iterate. The outer loop terminates the iterations as soon as the relative change between two successive

iterates satisfies

$$\|u^k - u^{k-1}\|_2 / \|u^{k-1}\|_2 < 10^{-4}.$$

The model (2) solved by (11)-(10) is strongly dependent on the choice of the  $\lambda$  parameter, which must be estimated correctly in order to obtain accurate solutions to the problem.

We propose to adopt an automatic estimation for  $\lambda$  which introduces an iterative *Outer continuation loop* which, starting from a reasonable value for  $\lambda^0$ , decreases its value properly, and uses it to solve at each iteration an iterative *Inner FB loop*.

This strategy, often successfully used under the name of *continuation* [19, 16], does not increase much the computing time of FB-scheme since each outer iteration uses as starting point the previous iterate (*warm starting*), and the stopping criterion in the inner loop (repeat loop) depends on the value of  $\lambda^i$ , namely  $\gamma \cdot \lambda^i$ , with  $\gamma \leq 1$ .

In the inner loop, the FB-scheme (11)-(10) is solved,  $E^k$  is a diagonal matrix with elements obtained by applying the function  $\eta(\cdot)$  in (5) to the gradient magnitude of the approximated vector  $u^k$ , and it is initialized as a zero vector. Then a correction to the solution is applied by implementing a FISTA acceleration technique [2]. At each iteration step  $k$ , this improves the estimate yielded by FB-scheme performing a specific linear combination with the unmodified previous iterate using coefficient  $\alpha_k$ . This preserves the computational simplicity of our scheme, but significantly improves its convergence speed.

In the rest of this section we provide details on the reduction rule for  $\lambda$  we adopted for each outer iteration. It is common to make use of the empirical reduction rule  $\lambda^{i+1} = r \cdot \lambda^i$ , where  $r \in (0, 1)$  is the reduction factor, which is usually chosen as  $r = 0.5$ . As has been pointed out in [30], this does not appear to be the optimum choice. Hence, in our work, we use an iterative updating of the parameter  $\lambda^i$  as

$$\lambda^{i+1} = \lambda^i \cdot \frac{\mathcal{F}(u^i; \lambda^i)}{\mathcal{F}(u^{i-1}; \lambda^{i-1})} \quad (15)$$

which is supported by the following results which guarantee the descent property of the functional  $\mathcal{F}(u; \lambda)$ .

#### Proposition 3

Let  $\lambda^{i-1}$  and  $\lambda^i$  be the two values of the  $\lambda$  parameter satisfying  $\lambda^{i-1} > \lambda^i$  and  $u^{\lambda^{i-1}}, u^{\lambda^i}$ , are the corresponding minimizers of (2). Then, the functional  $\mathcal{F}(u; \lambda)$  satisfies

$$\mathcal{F}(u^{\lambda^{i-1}}; \lambda^{i-1}) > \mathcal{F}(u^{\lambda^i}; \lambda^i). \quad (16)$$

#### Proof

From the definition of  $\mathcal{F}(u; \lambda)$ , and the characterization of  $u^{\lambda^i}$ , it follows that:

$$\begin{aligned} \mathcal{F}(u^{\lambda^{i-1}}; \lambda^{i-1}) &= \frac{1}{2} \|Au^{\lambda^{i-1}} - g\|_2^2 + \lambda^{i-1} \|Lu^{\lambda^{i-1}}\|_1 + \|E^{\lambda^{i-1}} Lu^{\lambda^{i-1}}\|_2^2 \\ &> \frac{1}{2} \|Au^{\lambda^{i-1}} - g\|_2^2 + \lambda^i \|Lu^{\lambda^{i-1}}\|_1 + \|E^{\lambda^{i-1}} Lu^{\lambda^{i-1}}\|_2^2 \\ &\geq \frac{1}{2} \|Au^{\lambda^i} - g\|_2^2 + \lambda^i \|Lu^{\lambda^i}\|_1 + \|E^{\lambda^i} Lu^{\lambda^i}\|_2^2 = \mathcal{F}(u^{\lambda^i}; \lambda^i). \end{aligned}$$

□

## 5. METRICS AND RESULTS

In Section 5.1 we introduce the performance metrics used to evaluate the overall system, in Section 5.2 and 5.3 we compare Algorithm SR-SEG proposed in Section 4 for image super-resolution and segmentation, respectively. Finally, the statistical analysis in Section 5.4 will allow us to evaluate how the proposed post-processing pipeline affects the performance of the automatic Immunofluorescent Diagnostic System.

---

**Algorithm SR-SEG**


---

Inputs:  $g \in \Omega_L$ ,  $K$ ,  $\tau > 0$ ,  $\beta$  satisfying conditions in Prop. 2

Output:  $\hat{u}$  with  $K$  segmented regions.

$u^0 = A^T g$ ;

*Outer continuation loop*

**for**  $i = 0, 1, 2, \dots$  *until convergence* **do**:

$k = 0$

$t^k = 1$

*Inner Forward-Backward loop*

**repeat**

*Forward Step*

$$v^{k+1} = u^k - \beta(A^T(Au^k - g) + L^T E^k L u^k)$$

*Backward Step*

$$\tilde{u}^{k+1} = \text{prox}_{\beta\mathcal{R}}(v^{k+1})$$

*Correction of the solution*

$$t^{k+1} = (1 + \sqrt{1 + 4(t^k)^2})/2, \alpha_k = \frac{t^k - 1}{t^{k+1}}$$

$$u^{k+1} = \tilde{u}^{k+1} + \alpha_k(\tilde{u}^{k+1} - \tilde{u}^k)$$

**until**  $\frac{|\mathcal{F}(u^{k+1}; \lambda^i) - \mathcal{F}(u^k; \lambda^i)|}{|\mathcal{F}(u^{k+1}; \lambda^i)|} < \gamma \cdot \lambda^i$

*Update the parameter  $\lambda$  as in (15)*

*Update  $E$  as in (5)*

*Warm Starting:  $u^0 = u^{k+1}$*

**end for**

$\hat{u} = \text{Threshold}(u^{k+1}, K)$

---

### 5.1. Performance metrics

Before analyzing the numerical results, in this section we present some metrics that, given the nature of our problem, are aimed to provide diagnostically meaningful quality metric for the comparisons detailed in Section 5.4.

$M_1$  (*Sort Matching*). From the diagnostic point of view, we are interested both in the identification of the brightest spot in the image, which denotes the specific serotype present in the serum under analysis, and in the detection of other significant bright areas among the other spots, which identify the presence of cross-reactivity. Therefore, we order the four segmented spots on a given sampled image, following a decreasing concentration (intensity) order, and we compare the order obtained by the CMOS acquisition with respect to that obtained by the CCD acquisition of the same sample, considering the image captured by the CCD image sensor the ground-truth for the test. Let  $s_i$ ,  $i = 1, 2, 3, 4$ , be the calculated concentration in the  $i$ -th region, we count the positive matches, thus obtaining a matching score between 0 (no match) and 4 (full match). This score is a qualitative index that measures the correct ranking (order) of intensities among regions. We refer to this metric as  $M_1$  in the experimental Section 5.4.

$M_2$  (*Similarity Test*). The similarity between the four concentrations  $s_i$  detected by CCD and CMOS cameras, can be measured as the relative proportions among the corresponding intensities of the four spots in a given sampled image. Let  $\bar{s} = \frac{1}{4} \sum_{i=1}^4 s_i$ , be the mean value of the intensities over all the four detected spots in the sample image. Defining, for each spot, the variation in percentage

from the mean value  $\bar{s}$ , as

$$p_i = \frac{(s_i - \bar{s}) \cdot 100}{\bar{s}}, \quad i = 1, 2, 3, 4,$$

then the displacement between corresponding concentrations detected in CCD acquisition and those obtained by CMOS acquisitions is measured by

$$M_2 = \frac{1}{4} \sum_{i=1}^4 |p_{i,CCD} - p_{i,CMOS}|. \quad (17)$$

Smaller values for  $M_2$  identify better similarity between the two acquisitions.

$M_3$  (*Goodness-of-linear-fit*). To encourage the use of inexpensive CMOS sensors, with respect to CCD devices, we are interested in investigating if a map between the intensity values on the image captured by the CCD and those significantly lower captured by CMOS exists. For this purpose we construct the best linear fitting polynomials using regression analysis, then we determine how well the model fits the data by computing the goodness-of-fit R-squared ( $R^2$ ) statistic, also known as coefficient of determination. In particular, we compute the metric  $M_3$  as follows:

$$M_3 = 1 - R^2 = \frac{\sum_{i=1}^4 (s_{i,CCD} - \hat{s}_i)^2}{\sum_{i=1}^4 (s_{i,CCD} - \bar{s}_{CCD})^2}$$

where  $\hat{s}_i$  is the value predicted by the model in the  $i$ -th region. In general, the lower the  $M_3$  values, the better the linear model fits the data.

## 5.2. Results on image super resolution

In this section we evaluate the super-resolution performance of Algorithm SR-SEG, which implements a SISR method, on 2D synthetic and real images, and we provide a comparison with the most relevant state-of-the-art super-resolution methods, and with the classical Bicubic method [18]. In particular, we chose four representative SISR approaches, namely the methods TIP-ASDS-IR [13], ELAD-TIP14 [34], LANR-NLM [23], and NCSR [12]. The codes we used have been provided by the authors, and the parameters in the codes were chosen by trial and error to give the best results of each method. All the numerical computations are performed using MATLAB R2016b on an Intel i7-3770 CPU with 16 GB RAM.

The high resolution (HR) test images are shown in Fig. 2, and include both photographic images, namely *Butterfly*, *Cameraman* and *Satellite* ( $256 \times 256$ ), and geometric images such as *Geometric* ( $380 \times 380$ ), *Synthetic*, *Shape1*, *Shape2* ( $256 \times 256$ ), as well as a real image *Fluo-image* ( $64 \times 64$ ).

The low resolution (LR) images have been synthetically generated by their corresponding HR versions by applying a Gaussian blur operator, with bandwidth 7 and standard deviation 1.6, and finally downsampled by a factor  $s = 3$ .

We evaluated the super resolution results based on the Peak-Signal-to Noise Ratio (PSNR) and on Structural SIMilarity index (SSIM). In particular, PSNR is defined by

$$\text{PSNR}(u, \hat{u}) := 20 \log_{10} \frac{\max(\hat{u})}{\sqrt{MSE}} \text{ dB},$$

where  $u$  is an available approximation of the original HR image  $\hat{u}$  and  $MSE = \frac{1}{N^2} \sum_{i=1}^{N^2} (u_i - \hat{u}_i)^2$  represents the mean squared error. This measure provides a quantitative measure of the quality of  $u$ . A large PSNR-value indicates that  $u$  is an accurate approximation of  $\hat{u}$ ; however, the PSNR-values are not always in agreement with visual perception.

SSIM index, designed to improve on traditional methods such as PSNR and MSE, measures the similarity of image  $u$  using  $\hat{u}$  as the reference image, and it is defined as

$$\text{SSIM}(u, \hat{u}) = \frac{(2\mu_u \mu_{\hat{u}} + c_1)(2\sigma_{u\hat{u}} + c_2)}{(\mu_u^2 + \mu_{\hat{u}}^2 + c_1)(\sigma_u^2 + \sigma_{\hat{u}}^2 + c_2)} \quad (18)$$

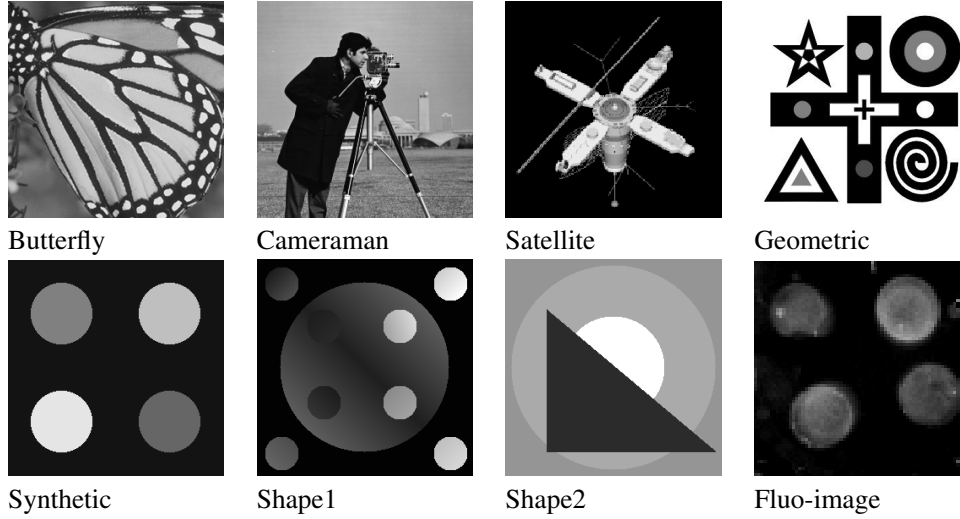


Figure 2. Test Images

Table II. Super-resolution results: PSNR (first row), SSIM (second row).

Image	Bicubic	[13]	[34]	[12]	[23]	OUR $E = 0$	OUR
Butterfly	21.36 0.7632	26.97 0.9028	26.72 0.8977	<b>27.75</b> <b>0.9111</b>	26.01 0.8681	26.75 0.9078	26.89 0.9097
Cameraman	22.90 0.7381	24.98 0.8251	24.90 0.8179	<b>25.27</b> <b>0.8259</b>	24.70 0.8110	24.73 0.8162	24.76 0.8168
Satellite	23.02 0.8347	25.50 0.9116	25.42 0.8879	26.03 0.9187	25.20 0.8819	26.20 0.9317	<b>26.25</b> <b>0.9322</b>
Geometric	19.13 0.7874	23.06 0.8760	24.95 0.8946	23.85 0.8696	23.90 0.8641	29.53 0.9703	<b>31.23</b> <b>0.9786</b>
Synthetic	25.90 0.9395	30.27 0.9791	30.48 0.9713	31.15 0.9799	29.30 0.9595	32.53 0.9887	<b>45.67</b> <b>0.9995</b>
Shape 1	28.30 0.9375	31.19 0.9706	31.49 0.9676	32.36 0.9512	30.4 0.9537	34.11 0.9852	<b>43.05</b> <b>0.9967</b>
Shape 2	27.22 0.9182	32.31 0.9681	32.13 0.9679	31.81 0.9748	31.91 0.9583	34.11 0.9852	<b>43.05</b> <b>0.9967</b>
Fluo-image	24.01 0.7656	29.08 0.9242	29.26 0.9186	28.48 0.9270	28.6 0.8857	29.58 0.9286	<b>29.74</b> <b>0.9299</b>

where  $\mu_u, \sigma_u^2, \mu_{\hat{u}}, \sigma_{\hat{u}}^2, \sigma_{u\hat{u}}$  are the local means, standard deviations, and cross-covariance for  $u$  and  $\hat{u}$ , respectively, and  $c_1 = (k_1 L)^2$ ,  $c_2 = (k_2 L)^2$  are two regularization constants, with  $L = 1$  and  $k_1 = 0.01, k_2 = 0.03$ .

In Table II we report for each test image the PSNR values (first row) and the SSIM index (second row), for every super-resolution method considered in the performance comparison. The last two columns report the performance results of the proposed super-resolution approach, (first part of Algorithm SR-SEG) named OUR, both setting  $\eta_i = 0, i = 1, \dots, N^2$  in  $E$  (marked as  $E = 0$  in Table), and updating the diagonal elements of  $E$  at each iteration by means of (5). We set the parameter  $\beta = 1.5$ , which satisfies the bound  $\beta \in (0, \frac{2}{\ell})$  following the condition proved in Prop. 2. The best PSNR/SSIM results are marked in boldface. The updating of the  $\eta_i$  allows for significant accuracy improvement with respect to the basic setting of all the diagonal elements zeros in  $E$ . In Table III we report the results of the comparisons in terms of execution times in seconds. From Table

Table III. Super-resolution results: execution times in seconds.

Image	Bicubic	[13]	[34]	[12]	[23]	OUR $E = 0$	OUR
Butterfly	0.028	135.14	8.47	179.11	31.8	5.27	11.01
Cameraman	0.028	118.18	8.67	168.18	31.4	3.52	16.10
Satellite	0.028	14.96	8.50	164.80	31.4	19.49	19.86
Geometric	0.036	219.32	15.80	283.11	49.1	6.08	6.10
Synthetic	0.028	108.20	8.67	154.29	31.5	3.36	3.37
Shape 1	0.028	109.38	9.14	156.21	31.9	3.97	3.33
Shape 2	0.028	115.98	8.39	162.13	31.8	3.43	3.44
Fluo-image	0.020	10.51	1.10	12.45	1.57	4.32	4.30

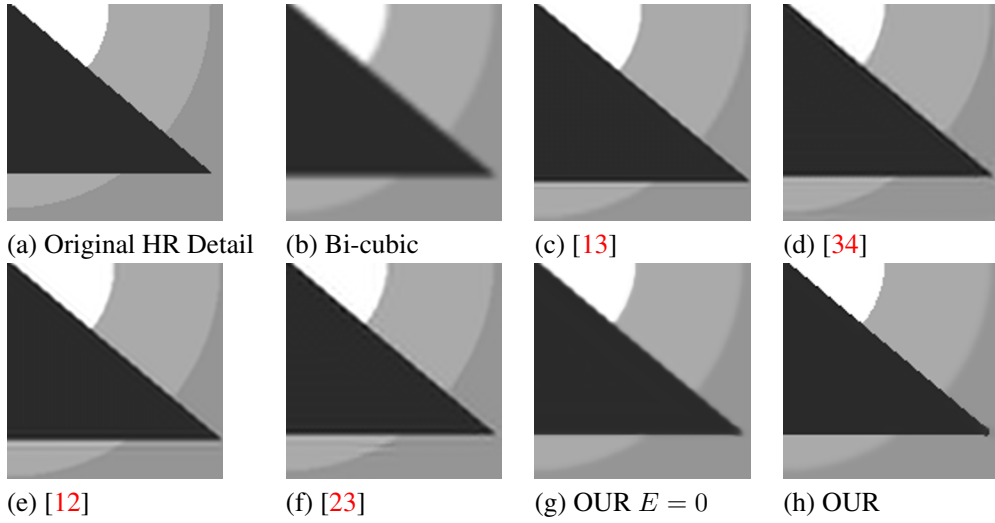


Figure 3. Super-resolution of Shape2 image: zoomed details of the resulting HR image.

**II** we can observe that the super-resolution results obtained by our model, specially in the case of synthetic images, outperform the results achieved by the other methods, both in terms of PSNR and SSIM, while maintaining very good computational efficiency.

Figure 3 shows a detail of the HR images obtained by enhancing the LR image Shape2 by the compared methods. The proposed method (OUR) achieves qualitative results which are visually more pleasing compared to the others, and reproduces sharper edges. In case of photographic images, the NCSR method (fourth column in Table II and III) leads to state-of-the-art performance, at the cost of a demanding computational time. The results obtained by the proposed method (OUR) in this scenario are quantitatively slightly lower but obtained in much less time, and in these cases, the use of  $\eta$  does not measure significant improvements. However, the computational time represents a strategic requirement in the overall evaluation of the Immunofluorescent Diagnostic System and the NCSR method is on average the slowest among the selected super-resolution approaches.

In Fig. 4(a) we show a LR CMOS image of dimension  $14 \times 14$ , and in Fig. 4 (b)-(e) the HR images obtained by applying the super-resolution method OUR with upscaling factors  $s = 2, 3, 4, 6$ , respectively. The segmentation results obtained without and with the preliminary application of a ( $s \times$ ) super-resolution procedure to the LR image, are illustrated in Fig. 4 (f)-(l). As expected, the super-resolution facilitates the segmentation procedure and allows for detecting finer segmented boundaries.



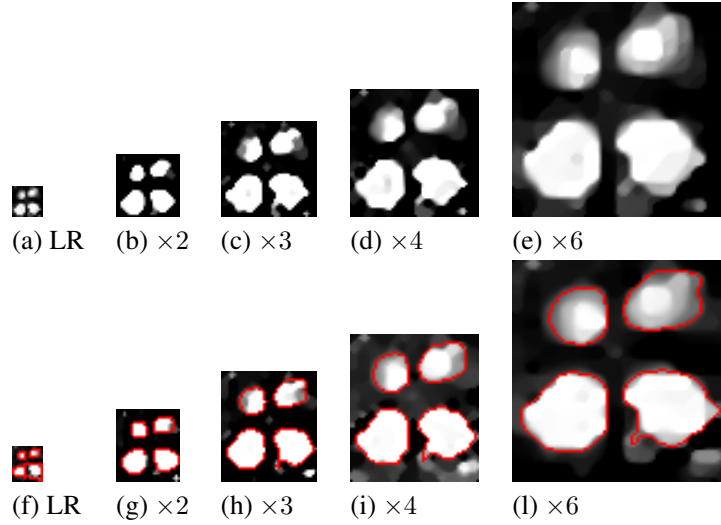


Figure 4. Results of Algorithm SR-SEG on a CMOS image: super-resolution, first row, segmentation, second row.

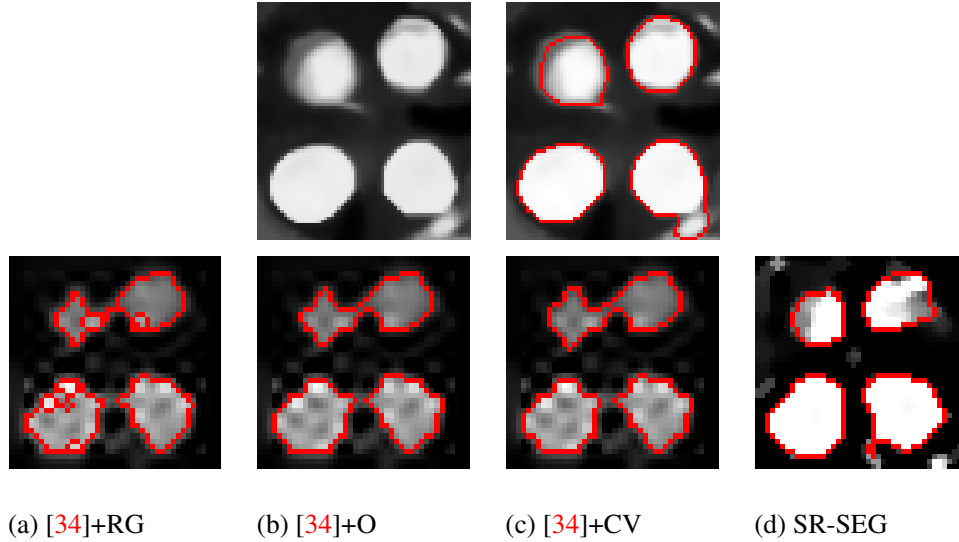


Figure 5. Segmentation results of the sample image 4478: (first row) CCD image and its segmentation by human expert; (second row) CMOS image and super-resolution + segmentation results. From left to right: (a)  $M_2 = 15.54$ , (b)  $M_2 = 12.53$ , (c)  $M_2 = 14.76$ , (d)  $M_2 = 4.44$ .

### 5.3. Results on image segmentation

In this section we evaluate the performance of the overall Algorithm SR-SEG when applied to real fluo-images acquired by the CMOS device. In order to define a quality measure of the segmentation results we consider as the best reference for the state-of-the-art Immunofluorescent Diagnostic procedure the images acquired using the high resolution CCD camera and then manually segmented by a human expert.

By the way of illustration, we report the results of two original input samples 4478 and 703, acquired by CCD camera and shown in Fig.5 and Fig.6 (first row, left), respectively; the corresponding manually obtained segmentation results are reported in Fig.5 and Fig.6 (first row, right), where the four boundaries of the regions segmented by the expert on the original background are red-colored.

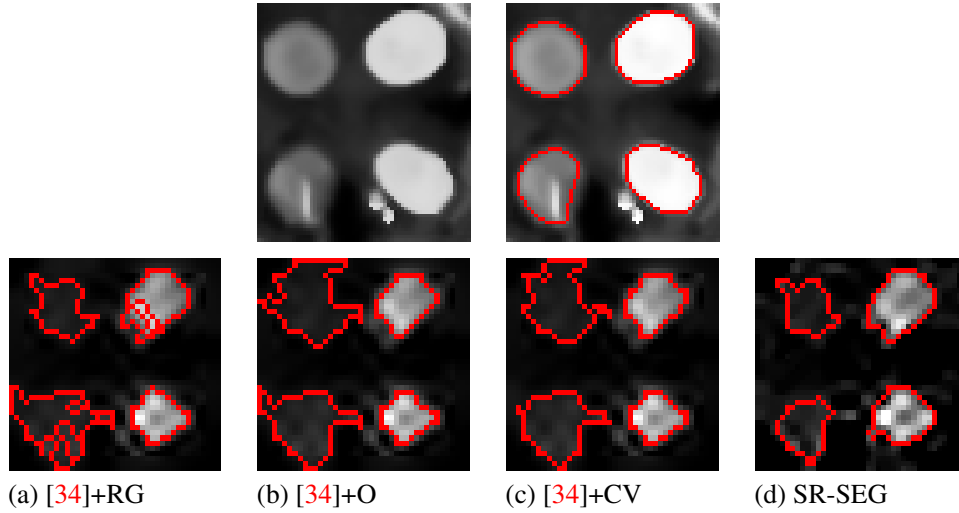


Figure 6. Segmentation results of the sample image 703: (first row) CCD image and its segmentation by human expert; (second row) CMOS image and super-resolution + segmentation results. From left to right: (a)  $M_2 = 34.68$ , (b)  $M_2 = 37.69$ , (c)  $M_2 = 35.81$ , (d)  $M_2 = 26.27$ .

From the diagnostic point of view, the two images analyzed here represent the antibodies IgG recognition of two real patients. The sample 4478 is from a patient affected by a secondary Dengue infection. In this case the patient has been infected by two or more Dengue serotypes and has developed a strong antibody reaction against different serotypes. It is evident from the image the very high spot intensities, as normal in secondary infections. The sample 703 is from a patient affected by a primary Dengue infection against serotype 2. The brightest spot correctly correspond to the right serotype while an important cross-reactivity can be observed with serotype 1.

In Fig. 5 and Fig. 6 (second rows, (a)-(c)), we illustrate the segmentation results obtained by first applying algorithm [34] with  $s = 3$  upscaling factor to enlarge the CMOS acquisitions, and then using other segmentation methods such as region growing (RG), Otzu (O) and Chan Vese (CV). In Fig. 5 and Fig. 6 (second rows, (d)) the results obtained by Algorithm SR-SEG are displayed for comparison.

From a qualitatively visual comparison, all the methods detect the four spots and all the segmented boundaries are acceptable even though they present significant visual differences with the human results on CCD illustrated in Fig. 5 and 6 (first row, right). However, the methods RG, O, CV fail to detect some inner parts of the regions, while the SR-SEG method is automatically tuned to consider as boundary a given gradient threshold suitably calibrated with the expert's sensitivity.

The threshold value represents a given grey-level above which the boundaries surrounding the spots in the image are considered salient in a given context. This parameter plays a fundamental role in selecting which pixels do not have to be considered as boundaries of segmented regions in the image. The thresholds can be set by the user or can be obtained automatically using any clustering method, such as the K-means algorithm. However, in our experience, once the camera is known, the grey-level intensities in the acquired fluo-images representing significant spots can be easily identified by an expert and then used to fix the threshold for the entire experimental session.

In addition to the visual inspection, for a quantitative evaluation of the performance of the competing methods, we provide in the captions of Fig. 5 and Fig. 6 (second rows) the values of the similarity metric  $M_2$  defined in (17), which confirm the higher quality of the proposed Algorithm SR-SEG.

The RG method is realized by the MATLAB function `regiongrowing.m`. Starting from a seed point (pixel) chosen by the user, this function accepts the neighbour pixel only if the difference between the pixel's intensity value and the mean of the already accepted region is lower than a

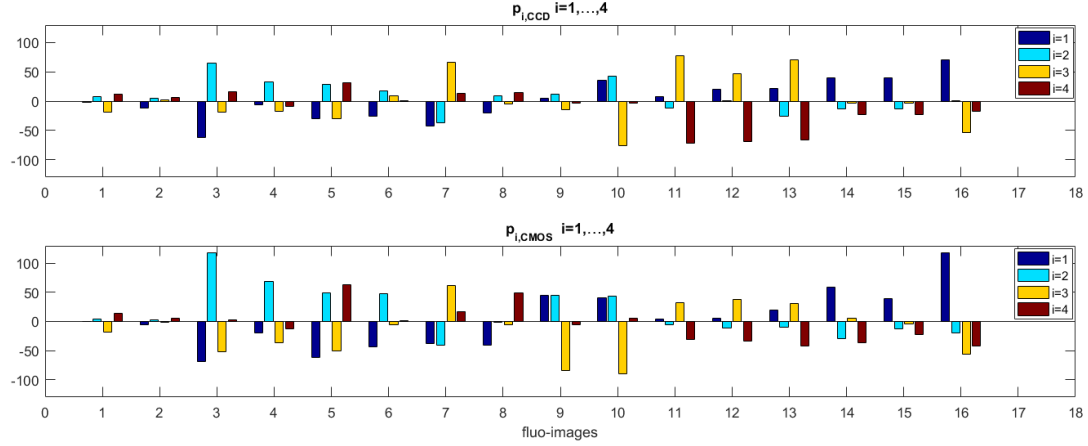


Figure 7. Distributions over the data set of the variations from the mean values  $p_{i,CCD}$  and  $p_{i,CMOS}$  used in  $M_2$  metric (17).

threshold value, fixed by the user. The weakness of RG methods is the manual choice of the seed pixels and the reduced capability to detect only connected regions [22, 38].

The Otsu's method, provided by the MATLAB command `graythresh.m` in the Image Processing toolbox, is a classical segmentation method (see [18]), which is based on finding the threshold that minimizes the weighted within-class variance or, equivalently, maximizing the between-class variance. It operates directly on the histogram of the image, so it is fast (once the histogram is computed), however it assumes homogeneous intensity and it does not make use of any spatial coherence which, in our Immunofluorescent Diagnostic System, is well known.

The CV method, introduced in [9], segments the input image by approximating it with a piecewise constant function and controlling the regularity of the boundaries. In our experiments we used the CV algorithm available in Image Processing Toolbox of MATLAB.

A key aspect analyzed to select the segmentation method within an image processing procedure is the robustness to the model parameters selection and the degree of human interaction, since the goal is to finalize an automatic diagnostic system. Regarding the regularization parameter choice, we have proposed an automatic estimate of  $\lambda$  in Section 4 which tunes the right parameter for the CMOS image sensor device.

RG method has the unavoidable limit of requiring both a thresholding value and manual interactions to locate the four seed points.

Otsu's method is quite automatic, but it can fail if the input image has not been enhanced in a proper way. Finally, the two variational methods CV and the proposed Algorithm SR-SEG are efficient and reliable and the involved free parameters can be easily and properly tuned in advance for each specific camera. From our experiments we noticed that, SR-SEG seems to be most robust for all the considered test images, it's fully automatic and integrates both super-resolution and segmentation procedures in a fast, reliable iterative process.

#### 5.4. Statistics for the metrics considered

We analyzed the performance of the overall diagnostic imaging system by exhibiting the statistics described in Section 5.1. The data set is composed by 16 fluo-images related to the detection of the Dengue virus serotypes acquired altogether by the CMOS and CCD cameras.

The *Sort Matching*  $M_1$  obtained is 100%. Since it represents the percentage of fluo-images that reach the full sort matching ( $M_1 = 4$ ) with respect to the diagnosis obtained by means of CCD acquisitions, this result confirms that our proposal represents a reliable alternative to the expensive state-of-the-art CCD based systems.

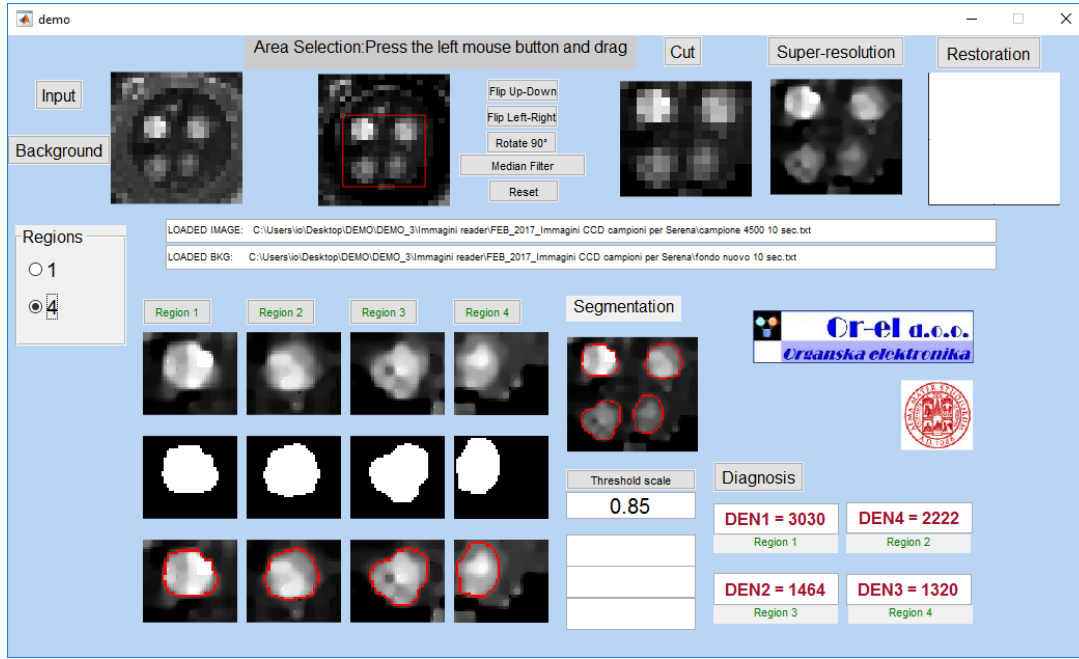


Figure 8. Demo software applied to the sample image 4500.

The result of the *Similarity Test*  $M_2$  metric calculated by the average value of the whole data set with respect to the diagnostic methods is 17.06. This low value represents a very good reproduction of the human performance on CCD images. For a better insight of the distribution of the values obtained on the entire data set, in Fig.7 we report the bar plots of the values of  $p_{i,CCD}$  (on the top) and  $p_{i,CMOS}$  (on the bottom) used in the computation of the  $M_2$  metric defined in (17). The four detected spots for each fluo-image are identified by different colors. The comparison between corresponding colored bars for each fluo-image in the two plots allows us to appreciate the good similarity also between corresponding spot intensities.

The *Goodness-of-linear-fit*  $M_3$  metric is 0.074. The final goal would be to have a function which maps the results produced by the specific P-CMOS device, into the CCD results. Even with a modest-size data set (16 images) the procedure proposed as post-treatment seems to produce results perfectly mappable by a linear map in those obtained by the CCD camera.

We can conclude that our Immunofluorescent Diagnostic System is accurate and reliable since it respects the right order of intensities wrt the CCD cameras, and reaches a very low value in terms of  $M_2$  and  $M_3$  metrics. The very good agreement between the relative spot intensity obtained with these two very different image sensors (CMOS and CCD) strongly motivates the replacement of the expensive CCD camera by the cheap P-CMOS, supported by the proposed Algorithm SR-SEG. According to the costs reported in Table I, this allows for a cost reduction up to 99%. All the sera in the considered data set have been analysed and tested with standard diagnostic methods: ELISA (two different commercial kits) and RT-PCR, confirming the diagnostic results obtained with our method. Moreover, considering that the proposed analysis time is about 30 minutes, including the sample preparation time and the running time for Algorithm SR-SEG ( $< 30secs$ ), compared with around two hours of ELISA and RT-PCR tests, and that the system is cheap, portable and can provide high precision results (high sensitivity and specificity), we can state that this diagnostic solution is very promising for these field applications.

This proposal have been implemented in a demo software realized to perform the automatic serotype Dengue recognition. An image of the demo panel is presented in Fig. 8. The restoration is applied only for images particularly noisy, which is not in general the case for CMOS fluo-images. The threshold used in Algorithm SR-SEG is automatically detected by K-means strategy. However,

once the camera used to acquire the fluorescent images is selected, a threshold scale parameter can be set to modify the threshold according to the expert's sensitivity.

## 6. CONCLUSIONS

In this work we presented an imaging procedure for an automatic computer-aided diagnosis in a fluorescence microscopy context. The introduction of this post-processing process is motivated by the goal of encourage the employment of more inexpensive CMOS cameras with respect to the high-sensitivity but more expensive CCD-based devices. The CMOS sensors used in this immunofluorescent application present problems due to their low spatial resolution. We proposed a novel variational model for spatially enlarging and segmenting the LR fluo-images. Numerical examples show that the proposed super-resolution approach is particularly effective and well suited for images characterized by sparse-gradient distributions and it is very competitive with respect to the state-of-the-art super-resolution methods. This model has been integrated in the two-phase pipeline procedure, where in the second stage the salient regions of interest in the fluo-image are analyzed by the diagnosis stage, in terms of quantitative detected concentration for a final classification. According to the introduced metrics and the performed experiments, the proposed immunofluorescent diagnostic system provided very good performance, in terms of accuracy, robustness and number of parameters to be set. The results obtained applying this image enhancing pipeline to the images acquired using a cheap, low resolution P-CMOS camera are then perfectly in line with the desired system sensitivity, considering the CCD images as the reference ones. Moreover, in addition to the reported tests, different experiments performed using the proposed analysis have confirmed the excellent ability of this system to correctly identify the right Dengue serotype, in particular for patients in convalescent phase [29].

A more accurate determination of the limit of detection of this new sensing scheme is envisaged in the next few months together with the possibility to define an antibody density calibration curve using calibrated blood samples. Finally, this diagnostic will be extended to IgM antibody since it is well known that this type of analysis provide the most precise Dengue serotype recognition.

## ACKNOWLEDGMENT

This work was supported by the “National Group for Scientific Computation (GNCS-INDAM)”, by ex60% project by the University of Bologna “Funds for selected research topics” and by ERC AdG project Multitherman.

## REFERENCES

1. A. Banerjee, Y. Shuai, R. Dixit, I. Papautsky, and D. Klotzkin. Concentration dependence of fluorescence signal in a microfluidic fluorescence detector. *Journal of Luminescence*, 130(6):1095 – 1100, 2010.
2. A. Beck and M. Teboulle. A fast iterative shrinkage-thresholding algorithm for linear inverse problems. *SIAM J. Img. Sci.*, 2(1):183–202, March 2009.
3. S. Bonettini, I. Loris, F. Porta, and M. Prato. Variable metric inexact line-search based methods for nonsmooth optimization. *SIAM Journal on Optimization*, 26(2):891–921, 2015.
4. S. Boyd, N. Parikh, E. Chu, B. Peleato, and J. Eckstein. Distributed optimization and statistical learning via the alternating direction method of multipliers. *Found. Trends Mach. Learn.*, 3(1):1–122, January 2011.
5. X. Cai, R. Chan, and T. Zeng. A two-stage image segmentation method using a convex variant of the mumford–shah model and thresholding. *SIAM Journal on Imaging Sciences*, 6(1):368–390, 2013.
6. Y. Cai, A. Smith, J. Shinar, and R. Shinar. Data analysis and aging in phosphorescent oxygen-based sensors. *Sensors and Actuators B: Chemical*, 146(1):14 – 22, 2010.
7. G. Casciola, D. Lazzaro, L. B. Montefusco, and S. Morigi. Shape preserving surface reconstruction using locally anisotropic radial basis function interpolants. *Comput. Math. Appl.*, 51(8):1185–1198, April 2006.
8. A. Chambolle. An algorithm for total variation minimization and applications. *Journal of Mathematical Imaging and Vision*, 20(1):89–97, Jan 2004.
9. T. F. Chan and L. Vese. Active contours without edges. *IEEE Transactions on Image Processing*, 10(2):266–277, Feb 2001.

10. E. Chouzenoux, A. Jezierska, J.-C. Pesquet, and H. Talbot. A majorize-minimize subspace approach for  $\ell_2 - \ell_0$  image regularization. *SIAM Journal on Imaging Sciences*, 6(1):563–591, 2013.
11. P. L. Combettes and V. R. Wajs. Signal recovery by proximal forward-backward splitting. *Multiscale Modeling & Simulation*, 4(4):1168–1200, 2005.
12. W. Dong, L. Zhang, G. Shi, and X. Li. Nonlocally centralized sparse representation for image restoration. *Trans. Img. Proc.*, 22(4):1620–1630, April 2013.
13. W. Dong, L. Zhang, G. Shi, and X. Wu. Image deblurring and super-resolution by adaptive sparse domain selection and adaptive regularization. *Trans. Img. Proc.*, 20(7):1838–1857, July 2011.
14. Shu PY et al. Dengue virus serotyping based on envelope and membrane and nonstructural protein ns1 serotype-specific capture immunoglobulin m enzyme-linked immunosorbent assays. *Journal of Clinical Microbiology*, 42(6):2489–2494, 2004.
15. F. Facchinei and J. S. Pang. *Finite-dimensional variational inequalities and complementarity problems*. Springer-Verlag, 2003.
16. M. A. T. Figueiredo, R. D. Nowak, and S. J. Wright. Gradient projection for sparse reconstruction: Application to compressed sensing and other inverse problems. *IEEE Journal of Selected Topics in Signal Processing*, 1(4):586–597, Dec 2007.
17. J.-M. Fritschy and W. Hrtig. *Immunofluorescence*. John Wiley & Sons, Ltd, 2001.
18. R. Gonzalez and Woods R. *Digital image processing*. Pearson Education, 2002.
19. E. T. Hale, W. Yin, and Y. Zhang. Fixed-point continuation for  $\ell_1$ -minimization: Methodology and convergence. *SIAM Journal on Optimization*, 19(3):1107–1130, 2008.
20. X. H. Han, J. Wang, G. Xu, and Y. W. Chen. High-order statistics of microtexton for hep-2 staining pattern classification. *IEEE Transactions on Biomedical Engineering*, 61(8):2223–2234, Aug 2014.
21. O Hofmann, XH Wang, JC deMello, DDC Bradley, and AJ deMello. Towards microalbuminuria determination on a disposable diagnostic microchip with integrated fluorescence detection based on thin-film organic light emitting diodes. *LAB ON A CHIP*, 5:863–868, 2005.
22. A. Javed, Y. C. Kim, M. C. K. Khoo, S. L. D. Ward, and K. S. Nayak. Dynamic 3-d mr visualization and detection of upper airway obstruction during sleep using region-growing segmentation. *IEEE Transactions on Biomedical Engineering*, 63(2):431–437, Feb 2016.
23. J. Jiang, X. Ma, Chen, T. Lu, Z. Wang, and J. Ma. Single image super-resolution via locally regularized anchored neighborhood regression and nonlocal means. *Trans. Multi.*, 19(1):15–26, January 2017.
24. B. Katchman, J. Smith, U. Obahiagbon, S. Kesiraju, Y.-K. Lee, B. O'Brien, K. Kaftanoglu, J. Blain Christen, and K. Anderson. Application of flat panel oled display technology for the point-of-care detection of circulating cancer biomarkers. *Scientific Reports*, 6(29057), 2016.
25. X. Li and M. T. Orchard. New edge-directed interpolation. *Trans. Img. Proc.*, 10(10):1521–1527, October 2001.
26. E. Fatemi L.I. Rudin, S. Osher. Nonlinear total variation based noise removal algorithms. *Physica D: Nonlinear Phenomena*, 60(1):259–268, 1992.
27. M. Manzano, F. Cecchini, M. Fontanot, L. Iacumin, G. Comi, and P. Melpignano. Oled-based dna biochip for campylobacter spp. detection in poultry meat samples. *Biosensors and Bioelectronics*, 66:271 – 276, 2015.
28. A. Marcello, D. Sblattero, C. Cioarec, P. Maiuri, and P. Melpignano. A deep-blue oled-based biochip for protein microarray fluorescence detection. *Biosensors and Bioelectronics*, 46:44 – 47, 2013.
29. P. Melpignano, E. Daniso, and N. Vidergar. Multiparametric oled-based biosensor for rapid dengue serotype recognition with a new point-of-care serological test. *Journal of Microelectronics, Components and Materials*, 46(4):250–256, 2016.
30. L. B. Montefusco and D. Lazzaro. An iterative  $\ell_1$  based image restoration algorithm with an adaptive parameter estimation. *IEEE Transactions on Image Processing*, 21(4):1676–1686, 2012.
31. D. Mumford and J. Shah. Optimal approximations by piecewise smooth functions and associated variational problems. *Communications on Pure and Applied Mathematics*, 42(5):577–685, 1989.
32. H. Nakajima, Y. Okuma, K. Morioka, M. Miyake, A. Hemmi, T. Tobita, M. Yahiro, D. Yokoyama, C. Adachi, N. Soh, K. Nakano, S. Xue, H. Zeng, K. Uchiyama, and T. Imato. An integrated enzyme-linked immunosorbent assay system with an organic light-emitting diode and a charge-coupled device for fluorescence detection. *Journal of Separation Science*, 34(20):2906–2912, 2011.
33. A. Pais, A. Banerjee, D. Klotzkin, and I. Papautsky. High-sensitivity, disposable lab-on-a-chip with thin-film organic electronics for fluorescence detection. *Lab Chip*, 8:794–800, 2008.
34. T. Peleg and M. Elad. A statistical prediction model based on sparse representations for single image super-resolution. *Trans. Img. Proc.*, 23(6):2569–2582, June 2014.
35. J. Shinar and R. Shinar. Organic light-emitting devices (oleds) and oled-based chemical and biological sensors: an overview. *Journal of Physics D: Applied Physics*, 41(13):133001, 2008.
36. Silvia Villa, Saverio Salzo, Luca Baldassarre, and Alessandro Verri. Accelerated and inexact forward-backward algorithms. *SIAM Journal on Optimization*, 23(3):1607–1633, 2013.
37. J. Yang, J. Wright, T. Huang, and Y. Ma. Image super-resolution via sparse representation. *Trans. Img. Proc.*, 19(11):2861–2873, November 2010.
38. X. Zang, R. Bascom, C. Gilbert, J. Toth, and W. Higgins. Methods for 2-d and 3-d endobronchial ultrasound image segmentation. *IEEE Transactions on Biomedical Engineering*, 63(7):1426–1439, July 2016.